Additive Manufacturing 12 (2016) 108–120

Contents lists available at ScienceDirect

Additive Manufacturing

journal homepage: www.elsevier.com/locate/addma

Experimental validation of finite element modeling for laser powder bed fusion deformation

Alexander J. Dunbar[a,*], Erik R. Denlinger[b], Michael F. Gouge[b], Pan Michaleris[b]

[a] Department of Mechanical and Nuclear Engineering, The Pennsylvania State University, Alexander Dunbar 4420D P.O. Box 30, State College, PA 16804, USA
[b] Autodesk Inc., USA

ARTICLE INFO

Article history:
Received 25 January 2016
Received in revised form 15 July 2016
Accepted 22 August 2016
Available online 30 August 2016

Keywords:
Finite element modeling
Additive manufacturing
Powder bed fusion
Distortion
Experimental validation

ABSTRACT

Experimental measurements are a critical component of model development, as they are needed to validate the accuracy of the model predictions. Currently, there is a deficiency in the availability of experimental data for laser powder bed fusion made parts. Here, two experimental builds of cylindrical geometry, one using a rotating scan pattern and the other using a constant scan pattern, are designed to provide post-build distortion measurements. Measurements are made using a coordinate-measuring machine which provides distortion profiles along the height of the part at four separate locations. Measurements show that for these cylindrical thin wall builds, there is no discernable effect on distortion from using the rotating versus constant scan patterns. Project Pan finite element modeling software is used to model each of the experimental builds. The simulation results show good agreement with experimental measurements of post-build deformation, within a 12% percent error as compared to experimental measurements. Using the FE model, the effect of a flexible versus a rigid substrate on distortion profile is examined. The FE model is validated against in situ experimental measurements of substrate distortion. The simulated results are used to study stress and distortion evolution during the build process. Internal stresses calculated by the model throughout the part are used in explaining the final part distortion. The combination of experimental and simulation results from this study show that the distortion of the top layer is relatively small (less than 30%) throughout the duration of the build process compared to the peak distortion, which occurs several layers below the most recently deposited layer. For these geometries once the part is built to a sufficient height, the peak distortion magnitude does not change.
© 2016 Published by Elsevier B.V.

1. Introduction

Recent developments in additive manufacturing (AM) allow for the rapid production of end-use parts without the need for significant post-build machining. In particular, the accuracy attainable by laser powder bed fusion (LPBF) AM allows for parts to be built with complex interior geometry previously unattainable by traditional manufacturing means. However, residual stresses caused by localized thermal gradients in the parts often result in build failures. Build failures include: delamination of layers, support structure fracture, part interference with the recoating mechanism, high levels of post-build distortion, voids in solid material, and lack of fusion of deposited material [1–3]. In order to mitigate the several types of failure associated with high levels of material deformation, an improved understanding of how deformation and residual stress accumulate in AM parts is needed.

Much of the experimental research is focused on the micro-scale, single lines and individual layers. Pohl et al. [4] varied laser scan pattern and speed for a single layer and used post-process experimental deflection results to compare and identify the best build parameters. Work shown by Kempen et al. [5] utilizes a new technique for in situ melt pool characterization. By analyzing the melt pool in situ, ideal processing parameters are selected by performing several single track tests. While experiments like these are useful in the determination of ideal processing parameters required to achieve fully dense and fused material, they do not address geometry dependent structural stresses that build up in full-scale LPBF built components.

While experiments may be informative to the LPBF build process, when extended to the larger scale this type of parametric analysis proves to be expensive. In these cases, simulation can be used to identify ideal parameters to be used in LPBF. Zhang et al.[6] performed an analysis on processing parameters for the LPBF build

* Corresponding author.
E-mail address: ajd315@psu.edu (A.J. Dunbar).

http://dx.doi.org/10.1016/j.addma.2016.08.003
2214-8604/© 2016 Published by Elsevier B.V.

process. The study focused on a W–Ni–Fe powder bed build where a model was used to determine processing parameters required to reach a user specified melt pool depth. Another study performed by Dai et al.[7] used simulations to predict melt pool size based off of an input laser energy density. The work focused heavily on measuring the size of the melt pool and determined that the melt pool dimensions are on the order of hundreds of microns for LPBF. These studies provide examples of how modeling can be used in the setup stages of LPBF to identify processing parameters for a specific build process without the need for expensive experiments.

Modeling of additive manufacturing has proven to be successful in improving the understanding of the distortion accumulation during the AM process and guiding the design process to reduce build failures [5,8–21]. For example, Denlinger et al. [22] demonstrates the utility that FE modeling can have in the prevention part distortion. Similar models are scarce in the powder bed field. Most models that are available are limited to simulating small build volumes or single layers [16,17], melt pool dynamics [7] or have limited their analysis to the thermal side of the LPBF process [6,14,16]. While each of referenced experiments provide utility to the field of additive manufacturing, none has demonstrated capabilities for part-scale modeling.

The aforementioned models are limited in implementation with powder bed AM systems in that they are too computationally expensive for application in full part-scale modeling of LPBF. Mesh refinement studies performed show that element size must be at least the size of the melt pool radius or temperature equations will not properly converge [8]. For general purpose FE software (e.g., ANSYS, Abaqus) at least four elements are required per heat source radius [16]. Therefore, models that are applicable to alternate AM processes, (e.g., Directed Energy Deposition) cannot be directly applied LPBF processes, as the heat source diameter is approximately 10 times smaller for LPBF as compared to Directed Energy Deposition. This reduction in heat source diameter results in a minimum 1000 fold increase in elements to capture a similar volume of material. Currently, there are two known available software packages that are capable of modeling part-scale LPBF: (1) Diablo [11] and (2) Project Pan. To accurately model part-scale LPBF, special consideration must be made to include the complex inter-layer effects, resulting from the complex thermal history of the parts [23]. For that reason, Project Pan is used, as it allows for accurate modeling of inter-layer effects.

Many studies focus on the micro-scale (single tracks or layers) of the LPBF process. While the smaller scale studies are necessary in defining the mechanics of LPBF, understanding how a larger part distorts as a result of the build process is an important step in build failure mitigation for LPBF. In contrast to the abundance of studies focusing on the melt pool, process parameters and microstructure, few have published final build geometry of LPBF made parts. Here, two experimental builds of a simple cylindrical geometry with differing scan patterns are deposited to measure final build geometry and distortion profiles for parts made with LPBF AM. In addition to experimental analysis, a finite element (FE) model is experimentally validated and applied. The experiment performed also provides necessary validation data for future LPBF models. The use of modeling software for this work is to help further understanding of stress and distortion evolution throughout the build process.

2. Experiment

2.1. Experimental setup

Two LPBF builds are used to measure the distortion profiles of parts made using the LPBF build process. Experiments are designed with similar cross-sectional geometry with the goal of studying the effects scan pattern orientation. Parts are designed to be modeled to allow for further analysis on the evolution of stress and distortion. By reducing the complexity of the part, analysis is made easier as part geometries are constant along the height of the part.

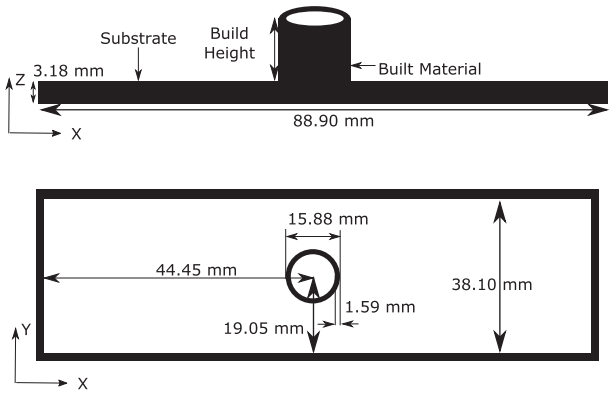

Fig. 1. Schematic of the deposition. Note that the build height is not constant for both cases. Build height for Case 1 (rotating scan pattern) is 6.16 mm. Build height for Case 2 (constant scan pattern) is 12.70 mm.

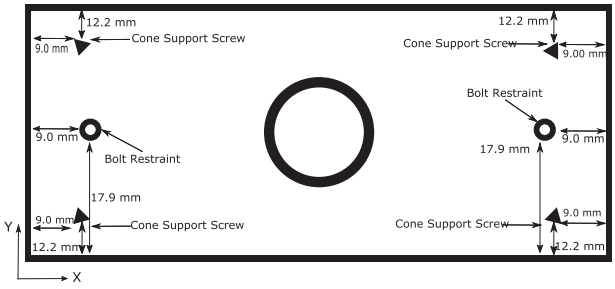

Fig. 2. Schematic of the constraints used to hold the substrates during the build process.

2.1.1. Description of experimental builds

Build dimensions and locations are defined by user created computer aided design (CAD) files. Builds are completed using interchangeable substrates. Interchangeable substrates allow builds to be removed from the LPBF machine without requiring post-build machining which will affect final build geometries. Fig. 1 is a schematic of build geometry and substrate for Case 1 and Case 2. The substrate dimensions are 88.9 mm × 38.1 mm × 3.18 mm in each case. Both cases are cylindrical geometries with an outer diameter of 15.88 mm and a cylinder wall thickness of 1.59 mm. As a result of a machine failure during production, build heights are 6.16 mm and 12.70 mm for Case 1 and Case 2, respectively. While the difference in part height prevents direct comparisons between the two cases, each case can still be analyzed as the build progressed properly until failure. Substrates are attached to the *vault* measurement system [23]. Substrates are constrained from underneath using restraining bolts that are threaded into holes on substrates, thereby restricting motion of the substrate without impacting the recoater mechanism. Substrates are supported in the corner using cone head set screws. Dimensions for constraints are shown in Fig. 2.

Fig. 3 shows the fully built material for Cases 1 and 2 with their substrates. In addition to differences in part height, Case 1 is built with the machine default rotating laser scan pattern and Case 2 is built with a constant scan pattern parallel with the *Y* axis. The rotating versus constant scan pattern are used to determine how alteration of this build parameter affects final build geometry. A schematic demonstrating a rotating versus constant scan pattern is

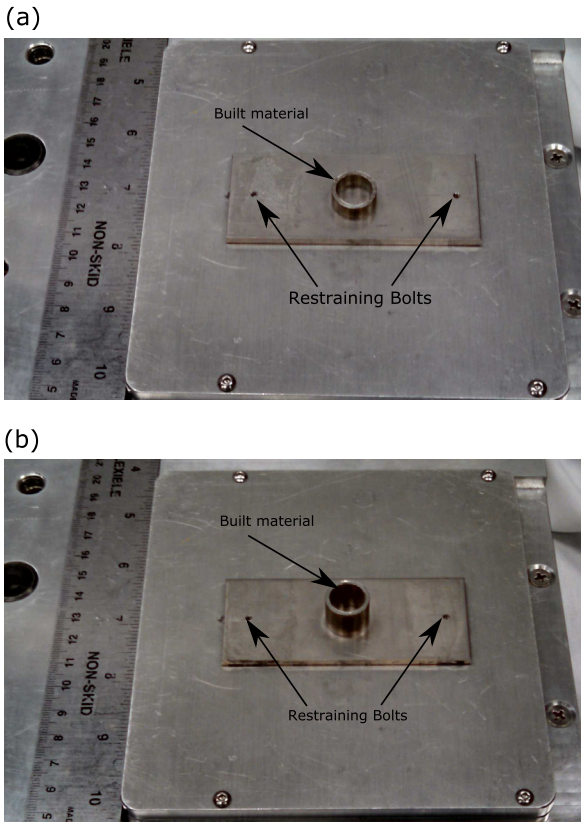

Fig. 3. Completed build with substrate for: (a) Case 1 (rotating scan pattern) and (b) Case 2 (constant scan pattern).

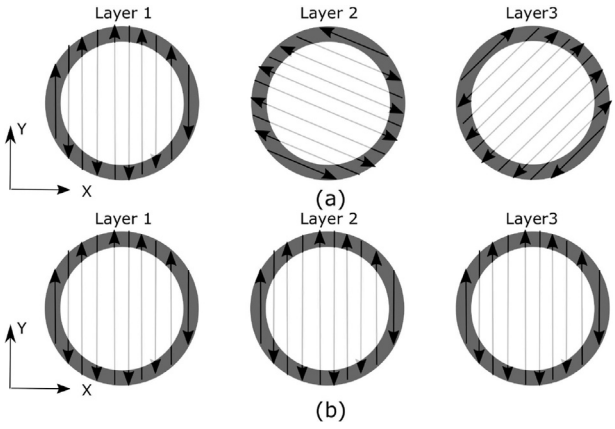

Fig. 4. Schematic of the scan pattern for: (a) Case 1 (rotating scan pattern) and (b) Case 2 (constant scan pattern).

Table 1
Description of experimental cases.

Case number	1	2
Material	Inconel®718	Inconel®718
Layer thickness (μm)	40	40
Laser speed (mm/s)	960	960
Hatch spacing (mm)	0.11	0.11
Rotating scan pattern	Yes	No

shown in Fig. 4. Descriptions of Case 1 and 2 processing parameters are summarized in Table 1.

The substrate and powder materials are both Inconel® 718. The average powder diameter is 30.4 ± 7/22 μm. Inconel® 718 is used as it is a common superalloy used in AM across several industries

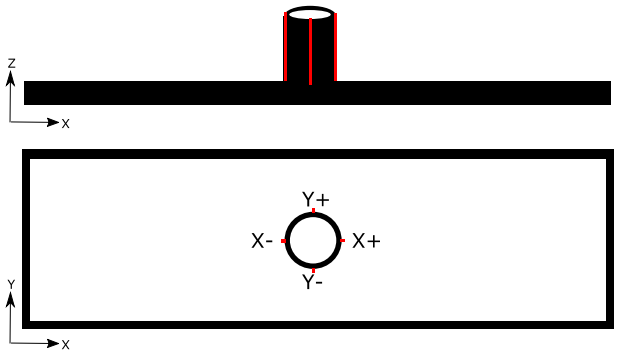

Fig. 5. Schematic of CMM measurement locations for Case 1 and 2.

[24–28]. Both cases are built using the EOS M280 LPBF machine. The EOS M280 machine uses a 4LR-400-SM-EOS laser that operates at a wavelength of 1060–1100 nm with a power of 400 W. Processing parameters used for these experiments include a layer thickness of 40 μm, a hatch spacing of 110 μm, a laser travel speed of 960 mm/s, and a laser power of 280 W.

2.1.2. Description of measurement equipment

Post-process measurements of the final build geometry are performed to quantify final distortion in each of the cases. A Core® RS-50 coordinate-measuring machine (CMM) is used to measure the outside walls of each cylinder at 4 separate XY positions for Case 1 and 2. The CMM uses a positive contact probe to measure the distortion profile along the height (*Z*) of the part. Measurement locations are shown in the schematic in Fig. 5. Measurement locations are labeled as +*X*, +*Y*, -*X*, and -*Y*, which correspond to the *X* and *Y* axis with an origin at the center of the build, these labels will be used when comparing and contrasting results. Measurements are made approximately every 0.05 mm along the height of the part. Measurements at the base of the part, lower than approximately *z* = 1.5 mm, were not captured due to the size of the measurement probe used. A recent calibration, completed in accordance ASME B894.1, Sections 5.3, 5.4.3, 5.5.2, and 5.5.4, shows a measurement accuracy of ±0.0044 mm over 1200 mm, ±0.0032 mm over 1000 mm, and ±0.0020 mm over 750 mm in the *x*, *y*, and *z* direction respectively. Distortion of the substrate during the build process is captured using a Lord Microstrain M-DVRT-3 connected to a DEMOD-DC 2 signal conditioner which translates displacements into voltages which are recorded using a National Instruments USB-6009 data acquisition (DAQ) system. This system provides in situ measurements of substrate distortion in the *Z* direction with an accuracy of ±15 μm. The measurement location for the *Z* distortion is found in Fig. 6.

2.2. Experimental results

Fig. 7(a) shows the experimental measurements for both Case 1 and Case 2 along the positive *X* measurement location (Fig. 5). In this study, distortion is defined as the difference between the prescribed and measured geometry for the specified measurement location. For both cases, oscillation in the distortion measurements is seen along the height of the part. Given the previously stated accuracy of the CMM machine, this is likely an effect of high surface roughness, which is common for metal powder based AM [29,30].

The distortion measurement for Case 1 at the positive *X* location distortion is nearly parabolic, with magnitude of distortion reaching a peak (0.10 mm) at only a single height (2.86 mm), whereas the distortion profile for Case 2 (constant scan pattern) has a nearly constant magnitude of distortion (0.92 mm) along much of the part height (from approximately 2 mm to 10 mm) when excluding

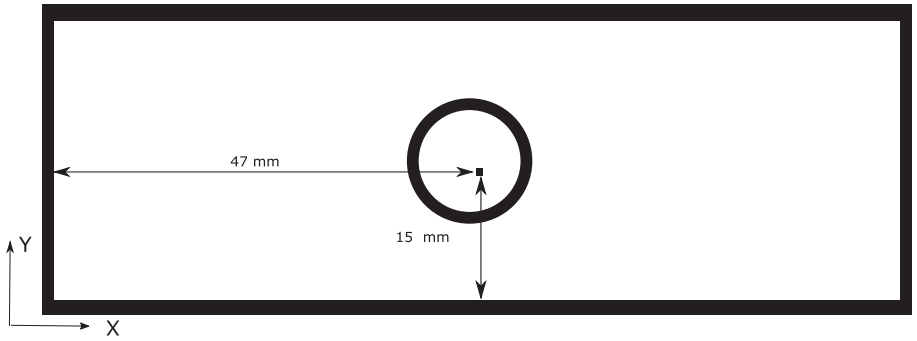

Fig. 6. Measurement location for in situ distortion measurements in the build direction (*Z*) during the build process.

oscillation due to surface roughness. Fig. 7(b) shows measurements at the positive *Y* measurement location. Consistent distortion shape profiles are seen for both Case 1 (rotating scan pattern) and Case 2 (constant scan pattern), with surface roughness affecting the measurements for Case 1 (rotating scan pattern) between a part height of 2 mm and 4 mm. Measurements of the negative *X* location are shown in Fig. 7(c). Similar shape profiles are again present for both Case 1 (rotating scan pattern) and Case 2 (constant scan pattern)as with Fig. 7(a) and (b). For both *X* measurement locations (Fig. 7(a) and (c)) indentations in distortion profile can be seen between build heights of 4–8 mm, this is not seen on either of the *Y* measurement locations (Fig. 7(b) and (d)). Measurements of the -*Y* measurement location, shown in Fig. 7(d), compare well with the other measurement locations with similar magnitude and shape for both cases. For both cases and each measurement location, the part distorts inward toward the center line of the cylindrical geometry.

Distortion values were compared for each of the four measurement locations at several heights along the part for both cases. At each height, a mean value of distortion is calculated, which is the averaged magnitude of the measured distortion between the four measurement locations. For those same heights, a percent deviation from this mean is calculated for each measurement location, to identify any trends in distortion profiles that may align with either the *X* or *Y* directions. These measurements are located in Tables 2 and 3 for Case 1 (rotating scan pattern) and Case 2 (constant scan pattern) respectively. To account for surface roughness, measurements at specified heights are averaged with the 5 measurement below and above selected height.

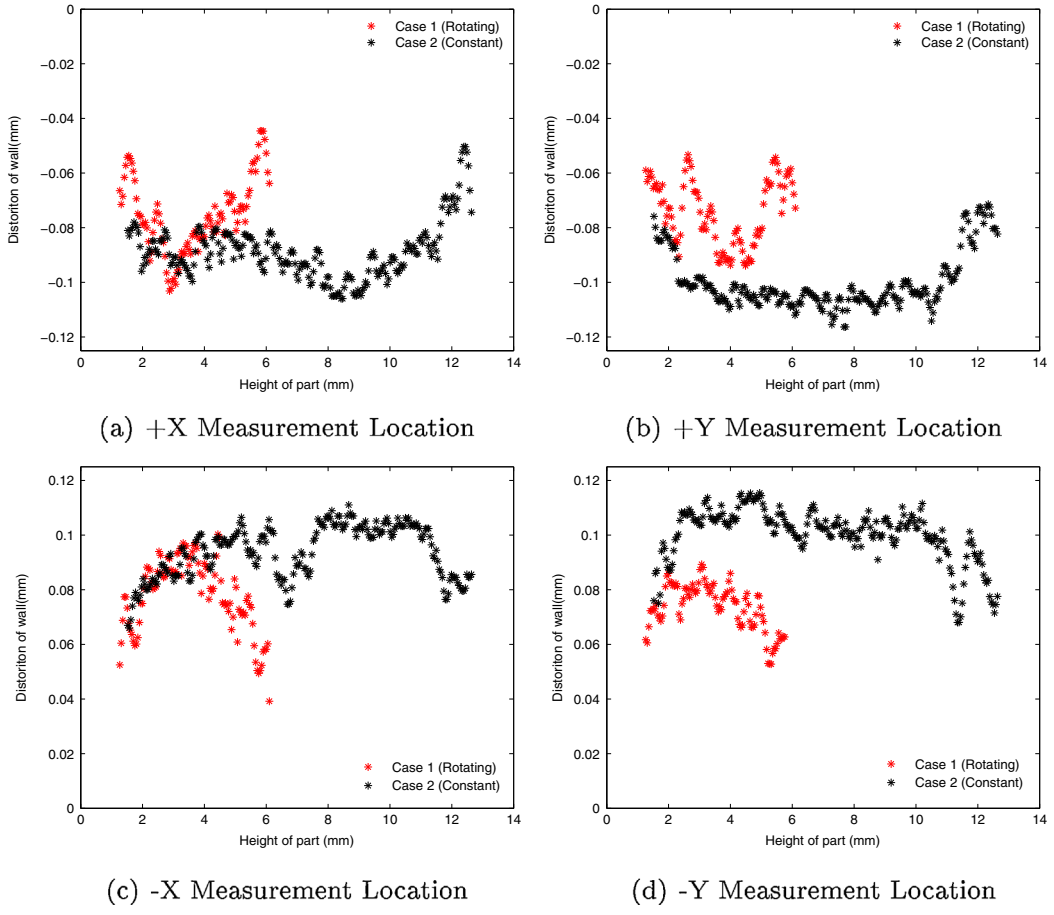

Fig. 7. Distortion measurement results along the four measurement locations for both Case 1 (rotating scan pattern) and Case 2 (constant scan pattern).

Table 2
Case 1 (rotating scan pattern) peak distortion comparison by percent deviation with experimental measurements.

Part height (mm)	Mean distortion magnitude (mm)	Positive X position (%)	Positive Y position (%)	Negative X position (%)	Negative Y position (%)
$Z = 2.0$	0.079	1.3	2.3	1.6	2.6
$Z = 3.0$	0.086	13.6	14.8	4.3	3.1
$Z = 4.0$	0.083	1.5	6.3	1.6	6.5
$Z = 5.0$	0.072	1.8	4.3	0.8	6.9
$Z = 5.5$	0.063	0.6	0.7	5.2	5.2

Table 3
Case 2 (constant scan pattern) peak distortion comparison by percent deviation with experimental measurements.

Part height (mm)	Mean distortion magnitude (mm)	Positive X position (%)	Positive Y position (%)	Negative X position (%)	Negative Y position (%)
$Z = 2.0$	0.087	1.7	1.6	7.5	7.3
$Z = 4.0$	0.098	12.7	7.8	3.3	8.1
$Z = 6.0$	0.099	10.7	8.8	0.4	1.3
$Z = 8.0$	0.103	1.4	2.3	2.2	3.2
$Z = 10.0$	0.102	6.8	1.5	1.3	4.0
$Z = 12.0$	0.082	13.3	1.8	1.0	14.1

Direct comparison cannot be made between experimental results of Case 1 and Case 2, as a result of their differing build heights but, within each case the four measurement locations can still be compared to each other. Tables 2 and 3 show that for both Cases 1 and 2 distortion measurements are consistent (under 15% difference) for each direction with no increased distortion trend aligned with either the X or Y directions. For Case 1, a rotating scan pattern is used, so isotropic distortion profiles are expected for each measurement location. For Case 2, all laser scans are aligned with the Y-axis (Fig. 4) so an asymmetry is expected for the distortion profiles. In particular, it is expected that the Y (longitudinal) distortion magnitudes would be larger than the X (transverse) distortion profiles [3]; however, no trend is found in the distortion profiles for Case 2 (constant scan pattern). Instead, large deviations found in any measurement location seem to be the result of localized defects, identified by large deviations from the mean distortion profile at only a single heights.

For each measurement location, distortion profiles for Case 2 (constant scan pattern) plateau at a part height of 3 mm, whereas the distortion profile for Case 1 (rotating scan pattern) reaches a peak distortion at one height resulting in a shape that is most nearly parabolic and where no plateau is reached. This is a result of their relative build heights where Case 1 is 6.16 mm tall and Case 2 is 12.70 mm tall. For the geometry used in these experiments, at a height of 4 mm, the rate at which distortion increases with height levels off until near the top of the part at approximately 10 mm. At low build heights the deposited material is constrained by the substrate thereby reducing the amount of distortion possible. As the part increases in height during the build process, the constraining effects of the substrate are minimized, and the part can distort freely. Distortion for these geometries is caused by the melted material of the current layer solidifying and compressing the material below it. For both cases, material near the top of the part distortion decreases rapidly as there are not enough layers above this point to cause significant distortion. To further examine these effects, an FE model is used to provide analysis and to help understand the distortion evolution throughout the build process.

3. Powder bed fusion simulation

The thermal and mechanical histories are determined by performing a three-dimensional transient thermal analysis and a three-dimensional quasi-static incremental analysis, respectively. The thermal and mechanical analyses are performed independently and are weakly coupled, meaning that the mechanical response has no effect on the thermal history of the workpiece [31].

3.1. Thermal analysis

The governing heat transfer energy balance is written as:

$$\rho C_p \frac{dT}{dt} = -\nabla \cdot \boldsymbol{q}(\boldsymbol{r}, t) + Q(\boldsymbol{r}, t) \tag{1}$$

where ρ is the material density, C_p is the temperature dependent specific heat capacity, T is the temperature, t is the time, Q is the volumetric internal heat generation rate, $\boldsymbol{x}$ is the relative reference coordinate, and $\boldsymbol{q}$ is the heat flux vector. The Fourier heat flux constitutive relation is:

$$\boldsymbol{q} = -k\nabla T \tag{2}$$

where k is the temperature dependent thermal conductivity.

Thermal radiation q_{rad} is calculated using the Stefan-Boltzmann law:

$$q_{rad} = \varepsilon\sigma({T_s}^4 - {T_\infty}^4) \tag{3}$$

where ε is the surface emissivity, σ is the Stefan-Boltzmann constant, and T_s is the surface temperature of the workpiece.

Newton's law of cooling calculates convective heat loss q_{conv}:

$$q_{conv} = h(T_s - T_\infty) \tag{4}$$

where h is the convective heat transfer coefficient.

3.2. Mechanical analysis

A quasi-static mechanical analysis is performed to calculate the mechanical response of the workpiece. The results of the thermal analysis are imported as a thermal load into the mechanical analysis. The governing stress equilibrium equation is:

$$\nabla \cdot \boldsymbol{\sigma} = \boldsymbol{0} \tag{5}$$

where $\boldsymbol{\sigma}$ is the stress. The mechanical constitutive law is:

$$\boldsymbol{\sigma} = \mathbf{C}\boldsymbol{\epsilon}_{\mathrm{e}} \tag{6}$$

Total strain $\boldsymbol{\epsilon}$, assuming small deformation thermo-elasto-plasticity, is decomposed as:

$$\boldsymbol{\epsilon} = \boldsymbol{\epsilon}_{\mathrm{e}} + \boldsymbol{\epsilon}_{\mathrm{p}} + \boldsymbol{\epsilon}_{\mathrm{T}} \tag{7}$$

Table 4
Temperature dependent thermal properties of solid Inconel® 718 [28,27].

T [°C]	k_s [W/m/°C]	C_p [J/kg]	ε_s
20	11.4	427	–
100	12.5	441	–
300	14.0	481	–
500	15.5	521	–
538	–	–	0.28
649	–	–	0.42
700	21.5	601	–
760	–	–	0.58
1350	31.3	691	–

Table 5
Temperature dependent mechanical properties of solid Inconel® 718 [24].

T [°C]	E (GPa)	σ_y (MPa)	α (μm /m °C)
21	208	1172	12.8
93	205	1172	12.8
204	202	–	13.5
316	194	–	13.9
427	186	1089	14.2
538	179	1068	14.4
649	172	1034	15.1
760	162	827	16.1
871	127	286	–
954	17.8	138	16.2

where $\mathbf{C}$ is the fourth-order material stiffness tensor, and $\boldsymbol{\epsilon}_e$, $\boldsymbol{\epsilon}_p$, $\boldsymbol{\epsilon}_T$, and $\boldsymbol{\epsilon}_t$ are the elastic, plastic, and thermal strain, respectively. The thermal strain is computed as:

$$\boldsymbol{\epsilon}_T = \boldsymbol{\epsilon}_T \boldsymbol{j} \tag{8}$$

$$\boldsymbol{\epsilon}_T = \boldsymbol{\alpha}(T - T^{ref}) \tag{9}$$

$$\boldsymbol{j} = \begin{bmatrix} 1 & 1 & 1 & 0 & 0 & 0 \end{bmatrix}^T \tag{10}$$

where $\boldsymbol{\alpha}$ is the thermal expansion coefficient and T^{ref} is reference temperature. The plastic strain is computed by enforcing the von Mises yield criterion and the Prandtl-Reuss flow rule:

$$f = \sigma_m - \sigma_y(\boldsymbol{\epsilon}_q, T) \leq 0 \tag{11}$$

$$\dot{\boldsymbol{\epsilon}}_p = \dot{\boldsymbol{\epsilon}}_q \boldsymbol{a} \tag{12}$$

$$\boldsymbol{a} = \left(\frac{\partial f}{\partial \boldsymbol{\sigma}}\right)^T \tag{13}$$

where f is the yield function, σ_m is Mises' stress, σ_Y yield stress, $\boldsymbol{\epsilon}_q$ is the equivalent plastic strain, and $\boldsymbol{a}$ is the flow vector.

3.3. Numerical implementation

The thermal and mechanical analyses are performed using Project Pan (version 2.81) by Autodesk Inc. The analyses are done in a series of time steps with the current time step taking the solution at the previous time step as the initial condition. At each time step, the discrete equilibrium equations are solved by using the Newton-Raphson method.

Table 4 lists the temperature dependent thermal properties for Inconel® 718. Table 5 list the mechanical properties of the material including the Elastic Modulus, E, yield stress, σ_y, and thermal expansion coefficient, α. Table 6 lists the as-used constant material properties and processing conditions for the analyses.

Loose powder that goes unmelted during the deposition process is not included as part of the analysis. Conduction into the powder is modeled by applying an artificial convective boundary condition on the model. The value for the convection coefficient applied on all surfaces is shown in Table 6. Simulations using varying convection coefficients h were run in order to determine the sensitivity of the model to this unknown parameter. The result of these studies show that for these build geometries, a 50% increase or decrease in the value of convection coefficient result in less than 1% difference on final distortion results shown in Fig. 8.

Table 6
As-used constant material properties and processing conditions.

Parameter	Value
Ambient temperature T_∞ [°C]	25 [23]
Convection coefficient h [W/m^2/°C]	8
Density ρ [kg/m^3]	8146 [28]
Laser absorptivity η	0.40 [32]
Poisson's ratio ν	0.30 [24]

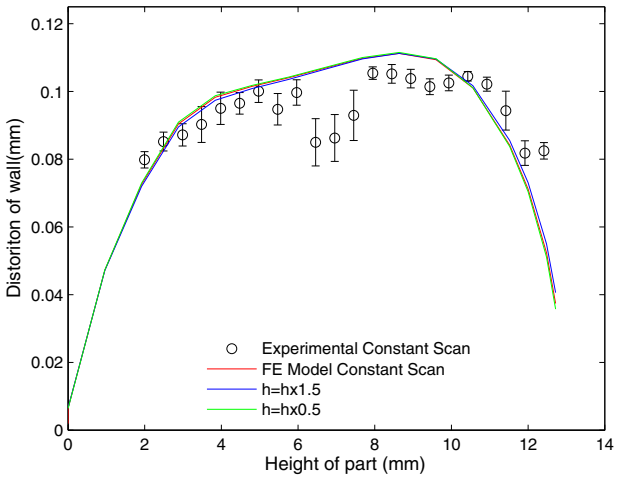

Fig. 8. Sensitivity of post-build distortion to FE model convection coefficient for constant scan pattern case (Case 2).

Fig. 9 shows the mesh used for the analysis. Meshing through Project Pan is done automatically with adaptive meshing allowing for coarse elements sufficiently far from the current layer and appropriate refinement where necessary for simulation accuracy. Three different mesh densities were simulated for each case to determine if the simulations were mesh independent. A mesh refinement study was completed for both temperature and distortion results, and for both cases the mesh used for the analysis demonstrated monotonic convergence with a peak difference of distortion magnitude under 2%.

The laser heat source Q is modeled using the double ellipsoid model [33]:

$$Q = \frac{6\sqrt{3}P\eta}{abc\pi\sqrt{\pi}} e^{-\left[\frac{3x^2}{a^2}+\frac{3y^2}{b^2}+\frac{3(z+vt)^2}{c^2}\right]} \tag{14}$$

where η is the absorbtion efficiency; x, y, and z are the local coordinates; a, b, and c are the transverse, depth, and longitudinal dimension of the ellipsoid respectively.

4. Results and discussion

4.1. Model comparison to experimental measurements

Simulation results were extracted at the experimental measurement locations (Fig. 5). For ease of comparison and to reduce noise from surface roughness, experimental measurements were averaged in groups of 10 with the standard deviation indicated by error bars. For these simulations, fixed substrate is used for mechanical boundary conditions. These boundary conditions prevent translation or distortion of the substrate. For the thermal

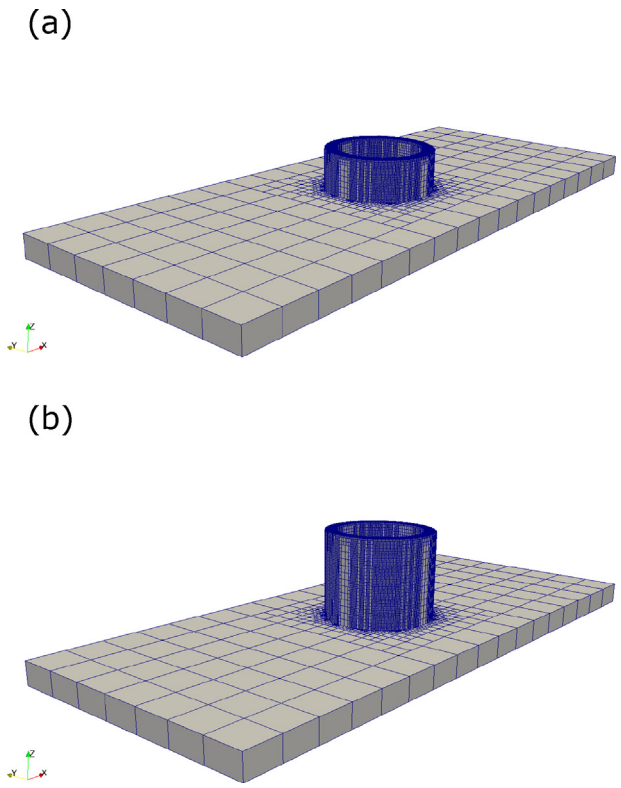

Fig. 9. Mesh used for: (a) Case 1 (rotating scan pattern) simulation (b) Case 2 (constant scan pattern) simulation.

analysis, initial conditions set the entire substrate to the ambient temperate (T_∞=25 °C).

A comparison between simulation results and experimental measurements for both Case 1 (rotating scan pattern) and Case 2 (constant scan pattern) can be found in Fig. 10(a) for the positive *X* location. Similar comparison for the experimental measurements and simulation results for the positive *Y* measurement location can be found in Fig. 10(b). Surface roughness, which cannot be captured by the model, affects the comparison between the model and experiments for Case 1 in Fig. 7(b) most notably at a height of 3 mm. Simulation results compared with experimental measurements are shown in Fig. 10(c) for the negative *X* location. A significant part defect, caused by earlier described surface effects common to AM, for Case 2 at a part height of 7 mm causes a localized discrepancy, but model results match experimental results outside of this region. The comparison for Case 1 is within measurement averaged standard deviation indicated by the error bars. The comparison of the simulation results and experimental measurements for the negative *Y* location is shown in Fig. 10(d). For each case, the FE model results match the experimental measurements well in both trend and magnitude.

For quantitative comparison between experiment and simulation, comparisons were made at along the height of the part in the FE model. Simulation results were averaged at each nodal height along the height of the part for each measurement locations (e.g. +*X*,+*Y*,-*X*,-*Y*). Comparisons for Case 1 and Case 2 are shown in Tables 7 and 8 , respectively. On average, FE model results compare well with experimental measurements with the largest difference between simulation results and experimental measurements as 12% at the +*X* measurement location for Case 2. Measurement locations with the largest percent errors correlate with previously discussed defects and roughness in experimental build surfaces.

Table 7
Comparison of experimental measurements and simulation results for Case 1 (rotating scan pattern). The error is averaged at each nodal location in the FE model along the height of the part for each measurement location (Fig. 5). Measurements are normalized by the experimental distortion measurement at each height.

Measurement location	Averaged error in FE model along the height of the part (%)
Positive *X* Position	6.2
Positive *Y* Position	10.2
Negative *X* Position	5.1
Negative *Y* Position	9.0

Table 8
Comparison of experimental measurements and simulation results for Case 2 (Constant scan pattern). The error is averaged at each node in the FE model along the height of the part for each measurement location (Fig. 5). Measurements are normalized by experimental distortion measurement at each height.

Measurement location	Averaged error in FE model along the height of the part (%)
Positive *X* Position	11.8
Positive *Y* Position	4.5
Negative *X* Position	7.6
Negative *Y* Position	7.6

4.2. Substrate deformation

Reviewing distortion measurements for Case 2 (constant scan pattern) for the positive and negative *X* measurement locations, an indentation in the distortion profile can be seen between a build height of approximately 4 mm and 8 mm. Simulations, shown in Fig. 10, modeled with a rigid substrate are unable to capture this feature in the distortion profile. To further investigate, a simulation with a flexible substrate that more closely matches the boundary conditions defined in Fig. 2 was completed. To match these constraints, translation in the *Z* direction is fixed at the cone set screw locations shown in Fig. 2. In addition, the *X*, *Y* and *Z* translations were fixed at the threaded bolt locations shown in Fig. 2. FE model results of the distortion of the substrate in the build direction (*Z*) are compared against in situ experimental measurements. A comparison of simulation results and experimental measurements of the distortion in the build direction is found in Fig. 11. At approximately 2400 s, the measurement equipment lost power and stopped recording, this is identified in Fig. 11 by a vertical dotted line. The model result for *Z* distortion is within 0.01 mm, placing it within 10% of the experimental measurement.

Results for each of the measurement directions are shown in Fig. 12. From the results shown in Fig. 12, it can be surmised that the localized indentation in the *X* measurement locations are likely caused by the distortion of the flexible substrate. This effect is likely driven by the *X* measurement locations being aligned with the long dimension of the substrate. As the substrate distorts in the negative *Z* direction, it causes an indentation in the cylinder wall. This result is concluded by comparing the *X* distortion profiles (shown in Fig. 12(a) and (c)) and the *Y* distortion profiles (shown in Fig. 12(b) and (b)). For the *Y* measurement locations, the inclusion of the flexible substrate does not not change the shape of the distortion profile, only the magnitude. However, for both of the *X* measurement locations, a distinct change in the distortion profile can be seen, which more closely matches the experimental distortion profile for the *X* direction. As no indentation is observed for Case 1 (rotating scan pattern), it is also likely that the indentation is also affected by part height. Inclusion of the flexible substrate in the simulation improves the accuracy as compared with experimental measurements. Table 9 presents quantitative results demonstrating improved accuracy of the flexible substrate simulation, using

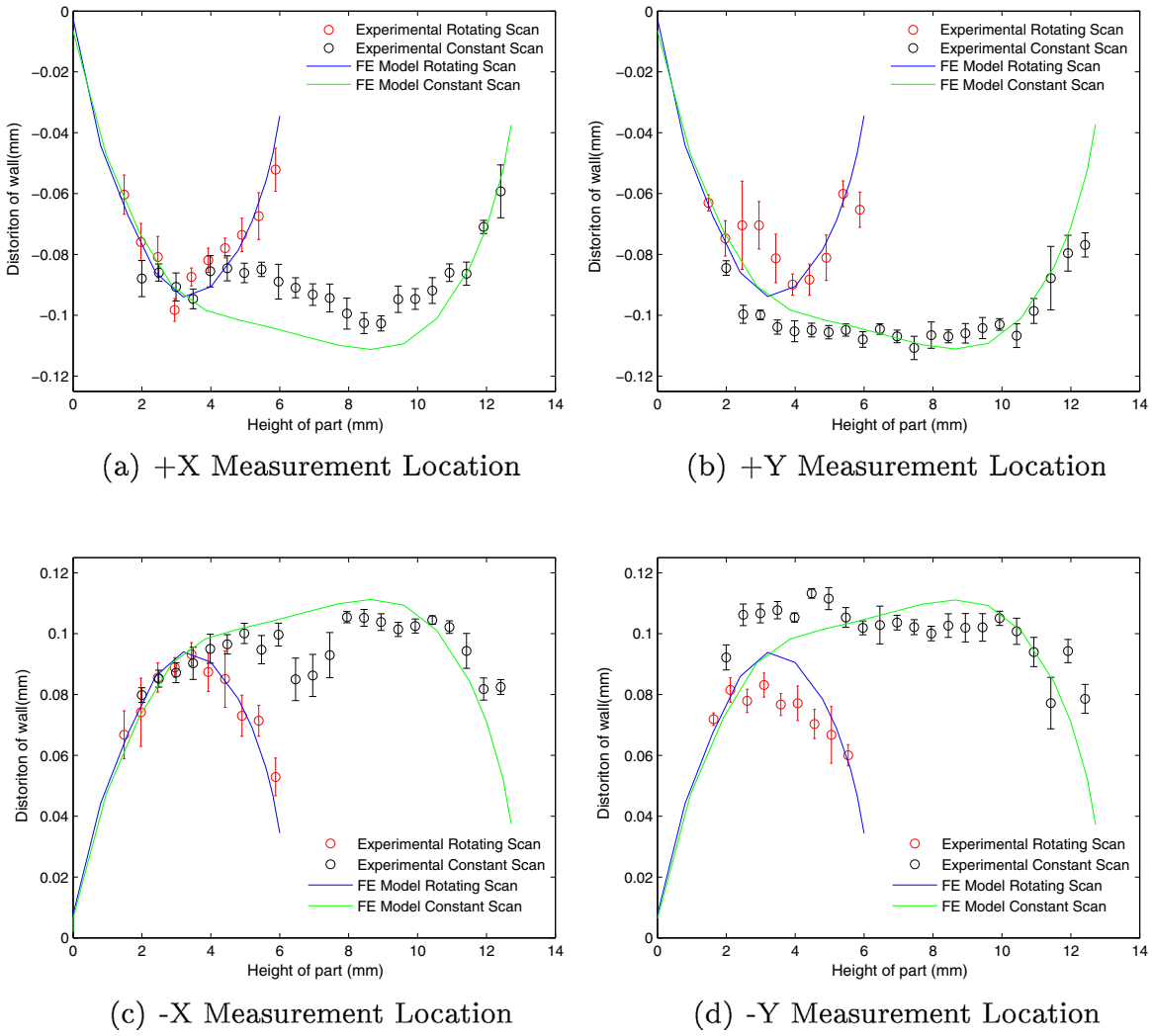

Fig. 10. Averaged CMM measurements of post-build distortion compared against FE model results at the four measurement locations shown in Fig. 5.

Table 9
Comparison of experimental measurements and simulation results for Case 2 (constant scan pattern) with and without a flexible substrate. The error is averaged at each node in the FE model along the height of the part for each measurement location (Fig. 5). Measurements are normalized by experimental distortion measurement at each height.

Measurement location	Averaged error in FE model along the height of the part fixed substrate (%)	Averaged error in FE model along the height of the part flexible substrate (%)
Positive *X* Position	11.8	8.6
Positive *Y* Position	4.5	7.8
Negative *X* Position	7.6	5.2
Negative *Y* Position	7.6	9.4

the previously described method for determining model accuracy to experimental measurements. Results shown in Table 9 show increased simulation accuracy in the Positive *X* and Negative *X* directions, but at a cost of accuracy in the *Y* directions.

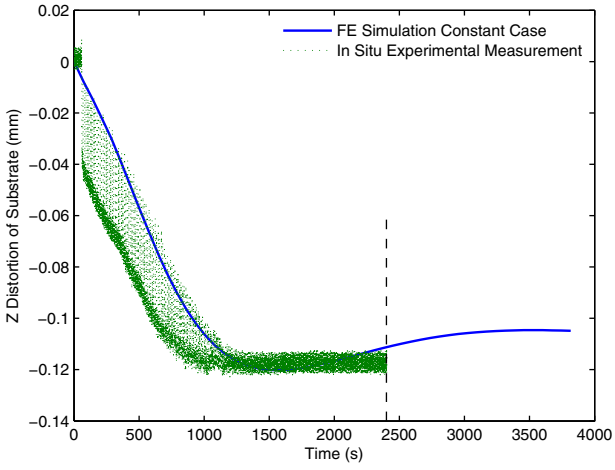

Fig. 11. Comparison of experimental and FE model results for distortion of the substrate in the build direction.

4.3. Extension of rotating scan pattern case

Due to a shortage of powder during the build process, the rotating scan pattern case was built shorter than designed. Using the previously validated model, the rotating scan pattern model was extended to its prescribed build height. The results of the extended rotating scan pattern case are shown in Fig. 13.

Results from these simulations (shown in Fig. 13) confirm previous statements regarding the minimal effect of rotating scan

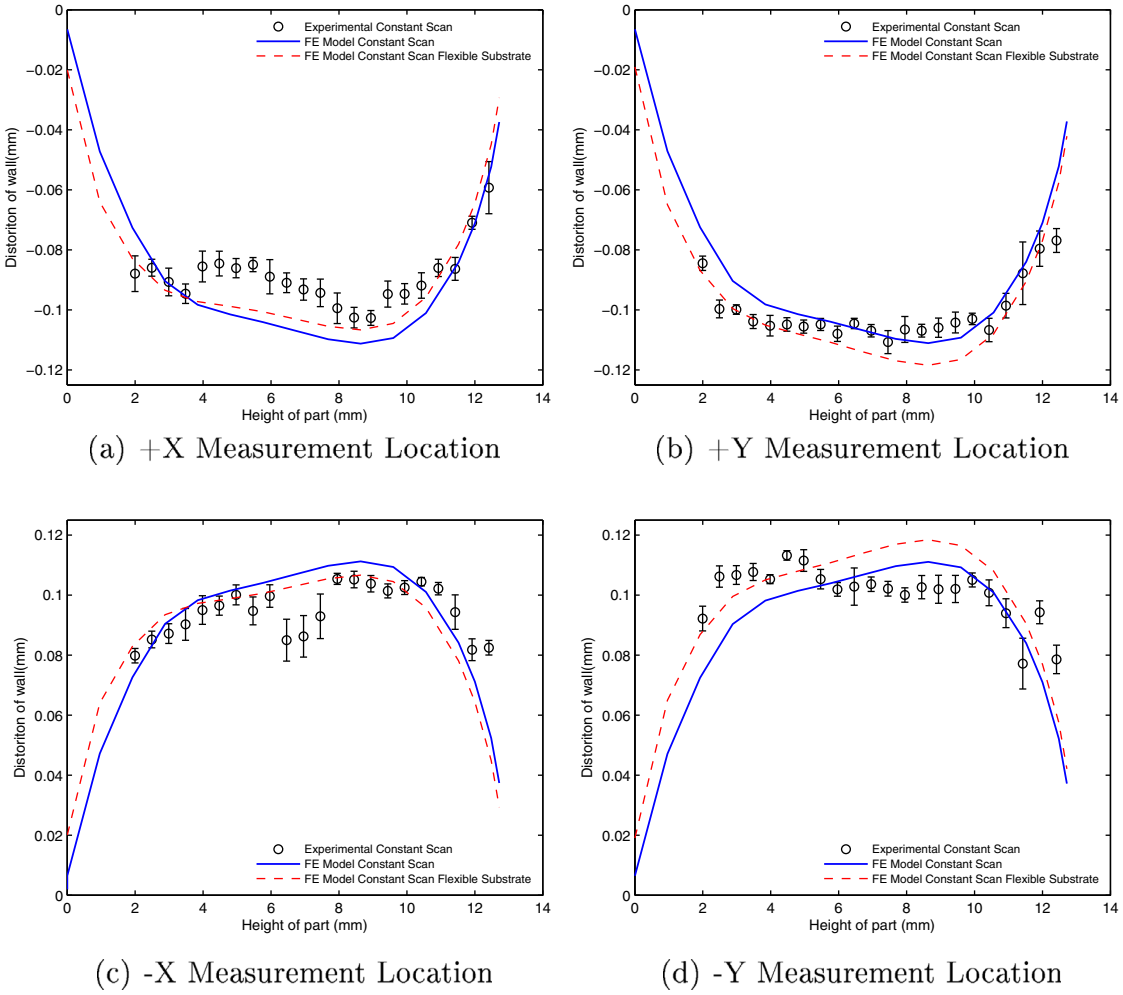

Fig. 12. Distortion results for simulation of Case 2 (constant scan pattern) with and without a flexible substrate for each of the four measurement locations shown in Fig. 5.

pattern for the thin-walled geometry presented. For each of the measurement locations, the rotating scan pattern consistently distorts less than the constant scan pattern, but the difference between the two cases are on average 1–2%, well within the models determined accuracy. The use of the FE model to provide a comparison of a part that was not successfully built with one that built correctly highlights another potential applications for FE model usage in LPBF AM.

4.4. Distortion evolution in time

For both cases, the final shape of the deposited cylinder flares out at the bottom where attached to the substrate, and the top where uncompressed by subsequent layers. Fig. 14 shows the simulation prediction of the build geometry, with distortion magnified 10 times, at the halfway (Fig. 14(a) and (c)) and final Fig. 14((b) and (d)) build time for Cases 1 and 2. The distortion magnitude for the constant scan pattern case (Case 2) indicates that at halfway through build, shown in Fig. 14(c)), the part has already reached the peak distortion magnitude, whereas for the rotating scan pattern, maximum distortion at halfway through the build (Fig. 14(a)) is lower than the final distortion values. The change in the profile of the part from Fig. 14(a) to (b) and Fig. 14(c) to (d) shows that the maximum distortion is not located at the top layer; rather, it is located at a height several layers beneath the top layer. This strengthens the conclusion that for this geometry, distortion is caused by the multiple layers solidifying and compressing layers previously built. The accumulation of stresses induced by the cooling and contracting of newly deposited material forces the middle height portion of the part into compression. For all four contour plots, distortion is a local minimum at the top layer whether halfway though the build or the finished build.

Fig. 15 compares the distortion value of the current top layer and the maximum distortion versus time for Case 2. At time $t = 4000$ s, the build process is completed, and the simulation allows the part to cool back to ambient temperature ($T = 25\,^{\circ}$C), causing the part to contract, resulting in an increase of the magnitude of the distortion profile. The importance of Fig. 15 is to demonstrate that from extremely early in the build (approximately $t = 100$ s) peak distortion is not at the top layer, but instead at a lower layer. Further confirming that distortion in these geometries is not a single layer effect, but instead it is the cumulative effect of multiple layers.

Fig. 16 shows the current height of the part and the height along the wall where the peak distortion is located for Case 2. Although, the location of the peak distortion continues to rise throughout the build process, it climbs slower than the height of the part.

For the majority of the build process, peak distortion is not found at the top layer, but instead at the layers below. During the build process, initially the peak distortion is located at the current layer, but once a sufficient part height is reached approximately (6.5 mm), the part height where the current peak distortion is located lags behind the height of the current layer. This can be seen in Fig. 16. Additionally, once the build progresses to approximately 2000 s (build height of 6.24 mm), the value of the peak distortion

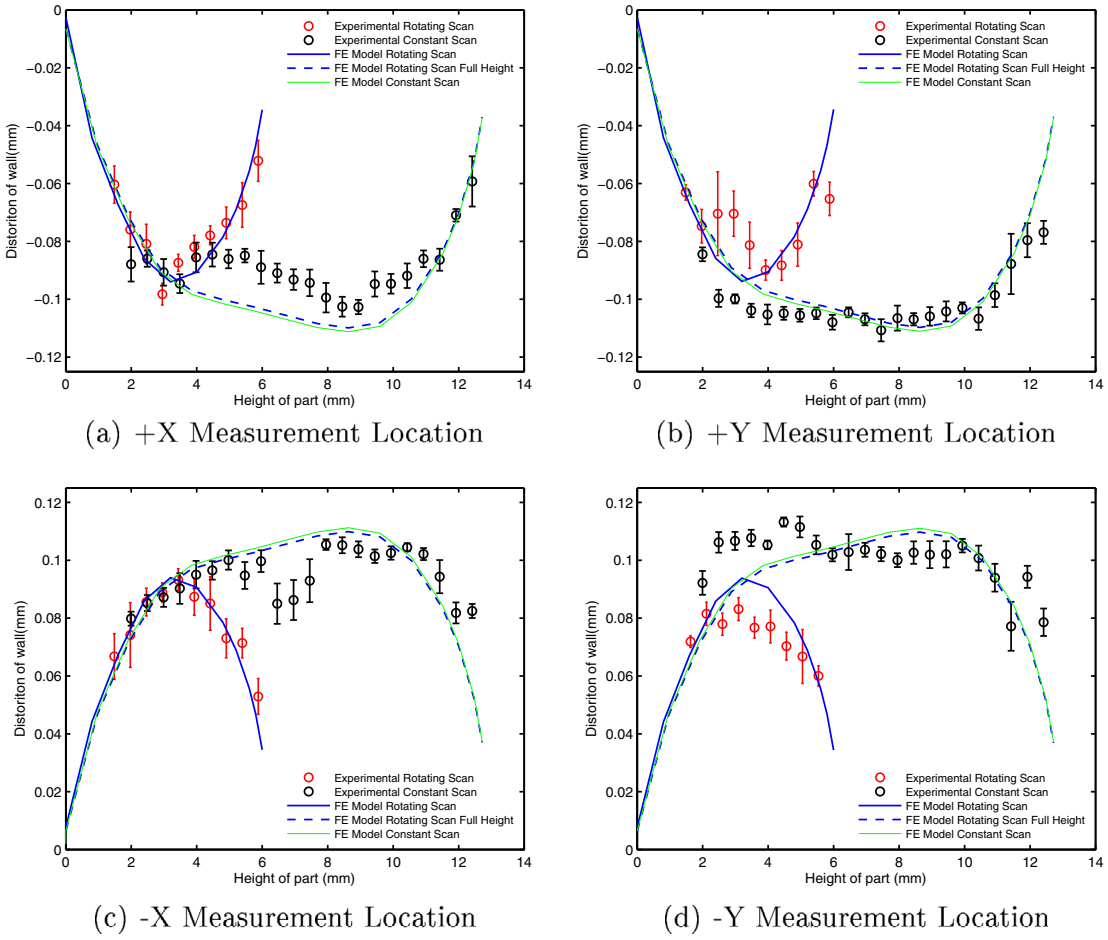

Fig. 13. Extension of the rotating scan pattern case to full build size for the four measurement locations shown in Fig. 5.

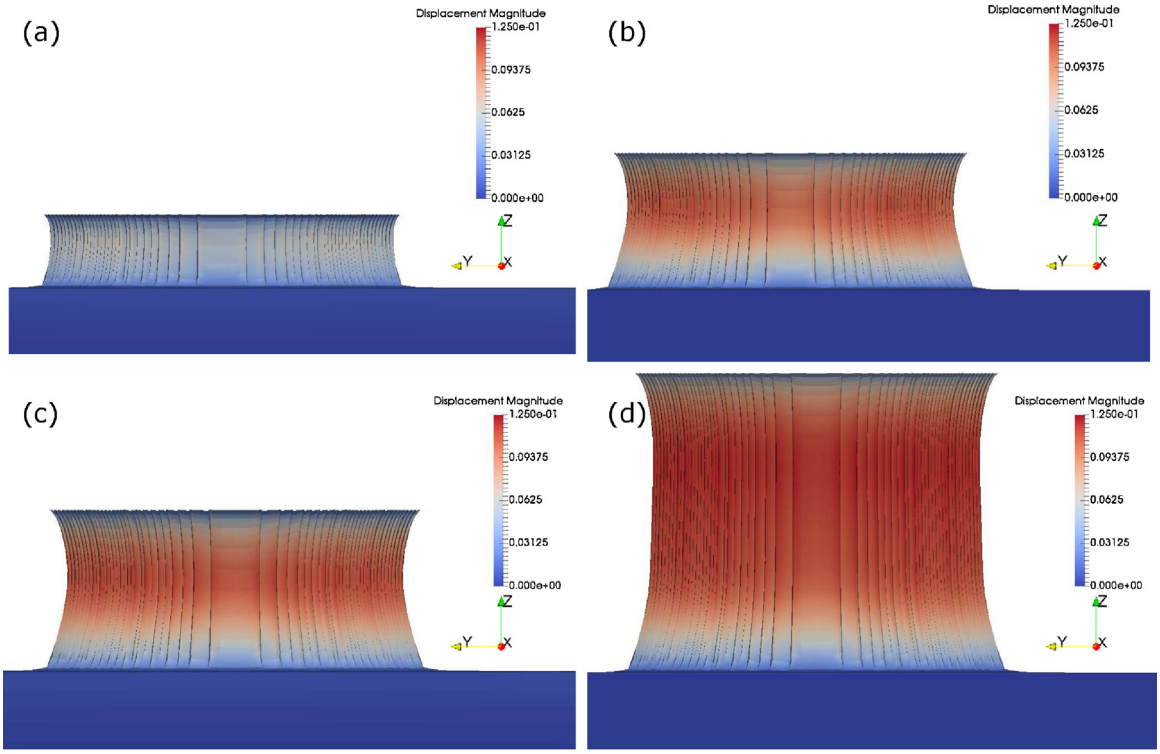

Fig. 14. Contour plots of distortion in mm (distortion magnified 10×) for: (a) Case 1 (rotating scan pattern) halfway through build, (b) Case 1 (rotating scan pattern) finished build after part has cooled to ambient temperature, (c) Case 2 (constant scan pattern) halfway through build, (d) Case 2 (constant scan pattern) finished build after part has cooled to ambient temperature.

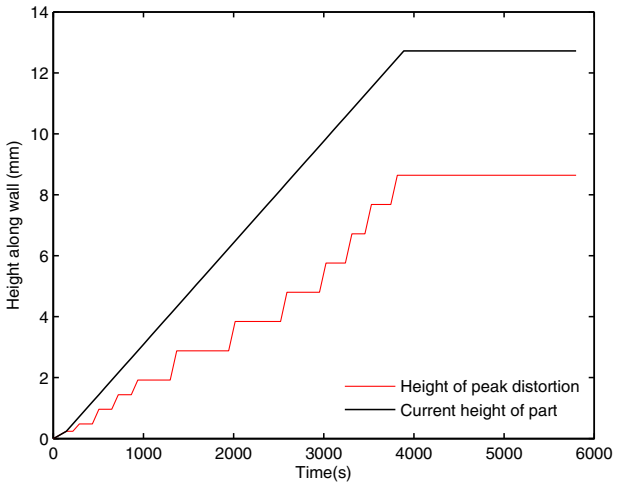

Fig. 15. Comparison of the current part height and peak distortion height versus time for the negative *X* measurement location for Case 2 (constant scan pattern).

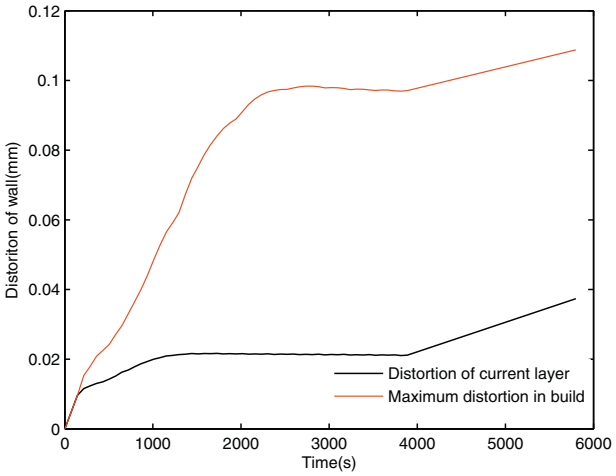

Fig. 16. Comparison of the distortion of the top layer and the peak distortion value versus time for the negative *X* measurement location for Case 2 (constant scan pattern).

plateaus. The plateau of distortion shown in Fig. 16 shows that once a sufficient build height is reached, peak distortion will become independent of part height. This effect determines the final shape of cylinders made in a LPBF build process which are flared out at the bottom and top of the part as the part restricted by the substrate below it and the top is relatively undistorted as there is no material above it to compress it. Results from the model give insight to distortion accumulation process and how currently added layers can affect previous layers.

Examining stress contours calculated by the model can help explain the final shape of the part. *X* and *Y* principle Cauchy stresses are shown in Fig. 17 at various heights through the build at halfway through the build process and for the completed part. Fig. 17 shows the bottom and top layers are in tension with high stress magnitudes. For each of the measurement locations, the distortion is

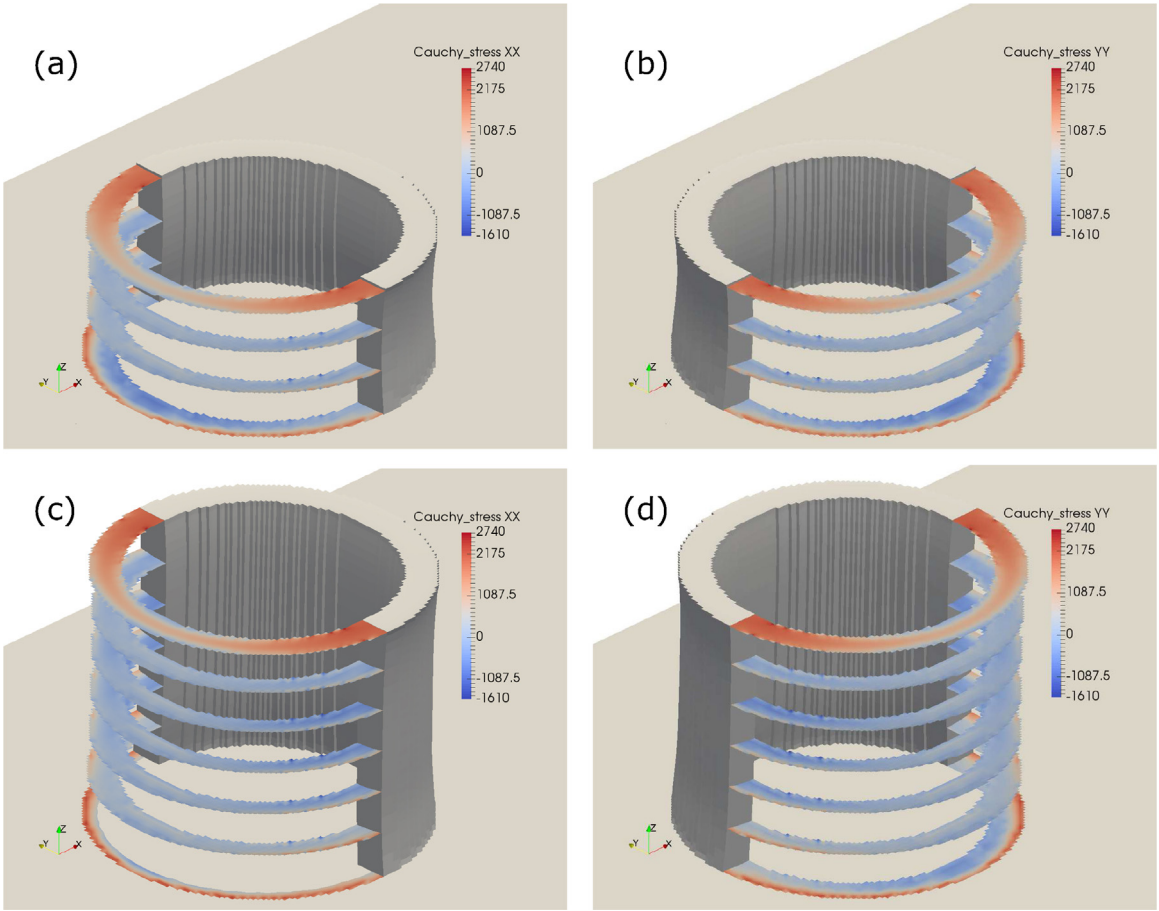

Fig. 17. Case 2 (constant scan pattern) contour plots of Cauchy stress in MPa (distortion magnified 2.5×) for: (a) Cauchy XX stress halfway through build halfway through build ($Z = 6.3$ mm), (b) Cauchy YY stress halfway through build ($Z = 6.3$ mm), (c) Cauchy XX stress for finished build and (d) Cauchy YY stress for finished build.

minimal at the top and bottom of the part. In the middle of the part compressive stresses dominate, reaching a maximum (approximately −1600 MPa) between a part height of 2 mm and 10 mm. Distortion reaches its peak magnitude in this region. Cauchy XX and YY stress profiles shown in Fig. 17(c) and (d), demonstrate this transition from tension at the bottom to compression throughout much of the part height back to tension at the top of the part. The result of this is a part that is undistorted at the top and bottom and with significant distortion between those section, resulting in an hourglass-like shape.

As is shown in Fig. 14, the built material final geometry resembles the previously described hourglass shape with distortion toward the centerline of the cylinder's geometry for the majority of the height of the part. When comparing Cauchy XX Stress (Fig. 17(a) with Fig. 17(c)) and Cauchy YY stress (Fig. 17(b) with Fig. 17(d)) for the halfway completed and fully completed builds, the maximum and minimum stress values at halfway through the build are within 5% of the completed build minimum and maximum stresses. Stress calculations are consistent with previous statements that the magnitude of distortion is independent of height, once a sufficient part height is reached for this geometry. For these parts, distortion and stress are caused by the accumulation of compression effects from multiple layers.

5. Conclusion

Two experimental builds with a simple cylindrical geometry are manufactured in a LPBF machine, one built with a rotating scan pattern and the other with a constant scan pattern, with the goal of providing measurements of the post-build distortion. CMM measurements of distortion show that for both cases, the parts distort towards the center line of the cylinder with approximately equal magnitude for each measurement location for both cases. Experimental measurements are compared against Project Pan FE model for validation purposes. FE model results compare well with experimental measurements made. The highest averaged percent error for any measurement location distortion profile falls within 12% of the experimental measurement.

Project Pan has been demonstrated effectively model in situ distortion of the substrate in the direction of the build height (Z) within 10%. By completing simulations using both a rigid and flexible substrate, it was determined that flexibility in the substrate affects the shape of the distortion profile for the X-direction. The inclusion of the flexible substrate for these simulations increases accuracy in the X measurement locations by 2–3% albeit at the cost of accuracy in the Y directions. Additional utility of the model is also demonstrated in extension of the rotating scan pattern case (Case 1), which was under-built due to complication during the build process. The FE model first validated on the experimental build of Case 1, extended the build height of that case to the predefined build height for comparison with the constant scan pattern (Case 2). Comparison of the model results for these cases show little discrepancy, further demonstrating that a rotating versus constant scan pattern does not have a significant impact on these geometries.

The FE model used for these simulation provides new information regarding the evolution of distortion during the build process. For these thin walled cylindrical geometries, distortion and residual stress accumulation is caused by solidifying material in the current layer compressing previous layers causing the part to distort inwards. As a result, distortion in the current top layer typically small (less than 30% of the peak distortion) during the build process and peak distortion is typically several layers below the top layer. Stress profiles calculated using the FE model are used to further explain the distortion profile along the height of the part.

Acknowledgements

Laboratory activities conducted during this research were conducted at the Center for Innovative Materials Processing through Direct Digital Deposition at Penn State. This material is based on research sponsored by Air Force Research Laboratory under agreement number FA8650-12-2-7230 and by the Commonwealth of Pennsylvania, acting through the Department of Community and Economic Development, under Contract Number C000053981. The U.S. Government is authorized to reproduce and distribute reprints for Governmental purposes notwithstanding any copyright notation thereon. Any opinions, views, findings, recommendations, and conclusions contained herein are those of the author(s) and should not be interpreted as necessarily representing the official policies or endorsements, either expressed or implied, of the Air Force Research Laboratory, the U.S. Government, the Commonwealth of Pennsylvania, Carnegie Mellon University, or Lehigh University. The authors would like to thank Schlumberger-Doll Research for their support of this effort. Any opinions, findings, conclusions, and/or recommendations in this paper are those of the authors and do not necessarily reflect the views of Schlumberger-Doll Research or its employees.

References

[1] J. Kruth, L. Froyen, J. Van Vaerenbergh, P. Mercelis, M. Rombouts, B. Lauwers, Selective laser melting of iron-based powder, J. Mater. Process. Technol. 149 (1) (2004) 616–622.
[2] I. Yadroitsev, P.h. Bertrand, I. Smurov, Parametric analysis of the selective laser melting process, Appl. Surf. Sci. 253 (19) (2007) 8064–8069.
[3] M.V. Deo, P. Michaleris, Mitigation of welding induced buckling distortion using transient thermal tensioning, Sci. Technol. Weld. Join. 8 (1) (2003) 49–54.
[4] H. Pohl, A. Simchi, M. Issa, H. Dias, Thermal stresses in direct metal laser sintering, in: Proceedings of the 12th Solid Freeform Fabrication Symposium, Austin, TX, 2001.
[5] K. Kempen, L. Thijs, J. Van Humbeeck, J. Kruth, Processing AlSi10Mg by selective laser melting: parameter optimisation and material characterisation, Mater. Sci. Technol. 31 (8) (2014) 917–923.
[6] D.Q. Zhang, Q.Z. Cai, J.H. Liu, L. Zhang, R.D. Li, Select laser melting of W–Ni–Fe powders: simulation and experimental study, Int. J. Adv. Manuf. Technol. 51 (5) (2010) 649–658.
[7] D. Dai, D. Gu, Thermal behavior and densification mechanism during selective laser melting of copper matrix composites: simulation and experiments, Mater. Des. 55 (2014) 482–491.
[8] E. Denlinger, J. Irwin, P. Michaleris, Thermomechanical modeling of additive manufacturing large parts, J. Manuf. Sci. Eng. 136 (6) (2014) 061007.
[9] E. Denlinger, J. Heigel, P. Michaleris, T. Palmer, Effect of inter-layer dwell time on distortion and residual stress in additive manufacturing of titanium and nickel alloys, J. Mater. Process. Technol. 215 (2015) 123–131.
[10] J.C. Heigel, P. Michaleris, T.A. Palmer, In situ monitoring and characterization of distortion during laser cladding of inconel® 625, J. Mater. Process. Technol. 220 (2015) 135–145.
[11] W. King, A.T. Anderson, R.M. Ferencz, N.E. Hodge, C. Kamath, S.A. Khairallah, Overview of modelling and simulation of metal powder-bed fusion process at lawrence livermore national laboratory, Mater. Sci. Technol. 31 (8) (2014) 957–968.
[12] P. Michaleris, Modeling metal deposition in heat transfer analyses of additive manufacturing processes, Finite Elem. Anal. Des. 86 (2014) 51–60.
[13] P. Michaleris, A. DeBiccari, Prediction of welding distortion, Weld. J.-Includ. Weld. Res. Suppl. 76 (4) (1997) 172s.
[14] R. Patil, V. Yadava, Finite element analysis of temperature distribution in single metallic powder layer during metal laser sintering, Int. J. Mach. Tools Manuf. 47 (7) (2007) 1069–1080.
[15] P. Peyre, P. Aubry, R. Fabbro, R. Neveu, A. Longuet, Analytical and numerical modelling of the direct metal deposition laser process, J. Phys. D: Appl. Phys. 41 (2) (2008) 025403.
[16] I.A. Roberts, C.J. Wang, R. Esterlein, M. Stanford, D.J. Mynors, A three-dimensional finite element analysis of the temperature field during laser melting of metal powders in additive layer manufacturing, Int. J. Mach. Tools Manuf. 49 (12) (2009) 916–923.
[17] C. Li, C.H. Fu, Y.B. Guo, F.Z. Fang, A multiscale modeling approach for fast prediction of part distortion in selective laser melting, J. Mater. Process. Technol. 229 (2016) 703–712.
[18] C. Li, C.H. Fu, Y.B. Guo, F.Z. Fang, Fast prediction and validation of part distortion in selective laser melting, Proc. Manuf. 1 (2015) 355–365.
[19] C. Li, J.F. Liu, Y.B. Guo, Prediction of residual stress and part distortion in selective laser melting, Proc. CIRP 45 (2016) 171–174.

[20] L. Papadakis, A. Loizou, J. Risse, J. Schrage, Numerical computation of component shape distortion manufactured by selective laser melting, Proc. CIRP 18 (2014) 90–95.
[21] F. Neugebauer, N. Keller, V. Ploshikhin, F. Feuerhahn, H. Köhler, Multi scale fem simulation for distortion calculation in additive manufacturing of hardening stainless steel, in: International Workshop on Thermal Forming and Welding Distortion, Bremen, Germany, 2014.
[22] E. Denlinger, J. Heigel, P. Michaleris, Residual stress and distortion modeling of electron beam direct manufacturing Ti–6Al–4V, in: Proceedings of the Institution of Mechanical Engineers, Part B: Journal of Engineering Manufacture, 2014, pp. 0954405414539494.
[23] A.J. Dunbar, E.R. Denlinger, J. Heigel, P. Michaleris, P. Guerrier, R. Martukanitz, T. Simpson, Development of experimental method for in situ distortion and temperature measurements during the laser powder bed fusion additive manufacturing process, Addit. Manuf. 12 (2016) 25–30.
[24] B.S. Yilbas, S.S. Akhtar, C. Karatas, Laser surface treatment of inconel 718 alloy: thermal stress analysis, Opt. Lasers Eng. 48 (7) (2010) 740–749.
[25] Z. Wang, K. Guan, M. Gao, X. Li, X. Chen, X. Zeng, The microstructure and mechanical properties of deposited-in718 by selective laser melting, J. Alloys Compd. 513 (2012) 518–523.
[26] G. Pottlacher, H. Hosaeus, E. Kaschnitz, A. Seifter, Thermophysical properties of solid and liquid inconel 718 alloy*, Scand. J. Metall. 31 (3) (2002) 161–168.
[27] V. Garcí, I. Arriola, O. Gonzalo, J. Leunda, et al., Mechanisms involved in the improvement of inconel 718 machinability by laser assisted machining (LAM), Int. J. Mach. Tools Manuf. 74 (2013) 19–28.
[28] D.G. Ahn, K.W. Byun, M.C. Kang, Thermal characteristics in the cutting of inconel 718 superalloy using CW Nd: Yag laser, J. Mater. Sci. Technol. 26 (4) (2010) 362–366.
[29] D. Thomas, The Development of Design Rules for Selective Laser Melting, University of Wales, 2009 (Ph.D. thesis).
[30] P.F. Jacobs, Rapid Prototyping & Manufacturing: Fundamentals of Stereolithography, Society of Manufacturing Engineers, 1992.
[31] L. Zhang, E.W. Reutzel, P. Michaleris, Finite element modeling discretization requirements for the laser forming process, Int. J. Mech. Sci. 46 (4) (2004) 623–637.
[32] C. Sainte-Catherine, M. Jeandin, D. Kechemair, J-P. Ricaud, L. Sabatier, Study of dynamic absorptivity at 10.6 μm (CO_2) and 1.06 μm (Nd-Yag) wavelengths as a function of temperature, Le Journal de Physique IV 1 (C7) (1991) C7–151.
[33] J. Goldak, A. Chakravarti, M. Bibby, A new finite element model for welding heat sources, Metall. Trans. B 15 (2) (1984) 299–305.